

Experimental observation of anomalous supralinear response of single-photon detectors

Josef Hloušek,* Ivo Straka, and Miroslav Ježek†

Department of Optics, Faculty of Science, Palacký University, 17. listopadu 12, 77146 Olomouc, Czechia

We demonstrate a direct single-source measurement of absolute nonlinearity of single-photon detectors with unprecedented accuracy. We discover a surprising supralinear behavior of single-photon avalanche diodes and show that it cannot be explained using known theoretical models. We also fully characterize sub- and supra-linear operation regimes of superconducting nanowire single-photon detectors and uncover the supralinearity under faint continuous illumination. The results identify new detector anomalies that supersede existing knowledge of nonlinear effects at the single-photon level.

I. INTRODUCTION

A majority of radiometric, spectroscopic, imaging, and optical communication methods rely on comparing two or more levels of light intensity measured by a photodetector and assuming that its response is proportional to the incident radiation. Transmittance measurement represents the simplest example where the optical power is detected with and without the sample under test, see Fig. 1(A). For an ideal detector, the power ratio would be the same as the actual transmittance of the sample. The measurement accuracy is, however, impaired by any deviation from a perfectly linear response of the detector. One can correct for the detection imperfections on the condition that the model of the nonlinear effect is known and accurate enough.

With the advent of ultra-sensitive detectors and quantum-enhanced metrology, we tend to perform measurements at the ultimate sensitivity levels dictated by the laws of physics [1, 2]. The goal is to reach the quantum advantage regime—that is, to improve the sensitivity of a measurement beyond the shot-noise limit, or to relax the requirements of the measurement, such as the minimum required detection efficiency. Shaping the statistics of light and using nonclassical optical signals as measurement probes allow for increasing the precision of length measurements [3, 4], imaging and particle tracking [5–9], and spectrophotometry [10, 11]. Optical transmittance measurement assisted by correlated photons and single-photon detectors can serve as a prominent example of a quantum-enhanced measurement scheme [12–15].

The measurement precision at the single-photon level is severely affected by the nonlinearity of the employed photonic detectors. The reason is that the other systematic errors need to be eliminated to reach the quantum regime, while the single-photon detectors themselves maintain strong inherent nonlinearity. One can observe a complex interplay of detector-specific phenomena, such as dark counts, dead time, recovery transition, multi-photon response, and latching. These effects cause highly

nontrivial nonlinear behavior that is much stronger compared to classical photodiodes—see Fig.1(B). Not only does the nonlinear response distort the measurement of the average photon flux, it also distorts the measured photon statistics and prevents us from reaching the ultimate precision of quantum-enhanced measurements. Notable experiments susceptible to detection nonlinearity are the tests of Born’s rule in quantum mechanics [16–21].

Here we explore the nonlinearity of actively and passively quenched single-photon avalanche diodes (SPADs) and a superconducting nanowire single-photon detector (SNSPD) for various bias currents. The employed nonlinearity measurement does not require a calibrated reference or time-resolved detection, which considerably simplifies the task. The nonlinearity characterization is performed with unprecedented accuracy; we reliably detect nonlinearities smaller than 1:1000, and cover seven orders of magnitude of incident illumination. We discover a supralinear region of SPAD operation, which is not consistent with any known theoretical models and has not been reported yet. We also characterize the nonlinear behavior of an SNSPD with a complex structure of sub- and supra-linear operation regions. We observed, for the first time, supralinearity of a SNSPD under continuous illumination at very low detection rates.

A. Single-photon detectors

Before discussing the main results, let us briefly review the fundamentals of single-photon detectors and basic principles of nonlinearity characterization.

A single-photon detector outputs an electronic pulse when one or more photons are detected [22–26]. The detection events (counts) arrive at random times with a statistical distribution given by the detected state and the response of the detector. The detection rate R^{det} is then a function of the incident rate R ; the rate is given in units of counts/s, or simply cps. Sometimes the detector outputs a pulse even when no photon is detected due to various background contributions (dark counts) or as a result of a previous detection (SPAD afterpulses). Furthermore, the detector occasionally fails

* hlousek@optics.upol.cz

† jezek@optics.upol.cz

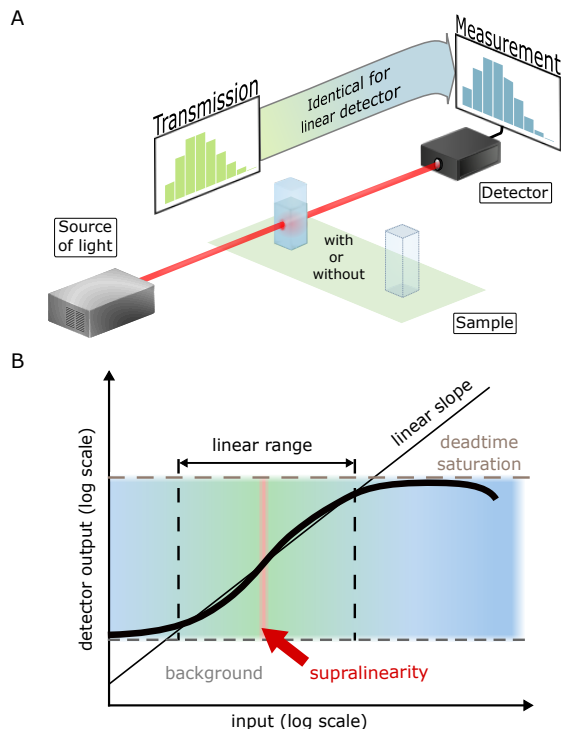


FIG. 1. (A) Optical transmittance measurement of a sample relies on comparing two levels of intensity captured by a detector. Any deviation from the ideal linear detection then critically affects the measurement accuracy. Nonlinearity is a particularly vexing problem in quantum metrology when nonclassical statistics of light is often required together with single-photon detectors. Their inherently nonlinear response distorts the photon statistics and makes it difficult to reach the quantum advantage. (B) Nonlinear behavior of a single-photon detector. Apart from the background detections and saturation effects, single-photon detectors may exhibit supralinearity.

to detect photons because it is not ready to do so after the previous detection event, such as during dead time or a latched state. Figure 1(B) illustrates the nonlinear behavior of a single-photon detector. A simple expectation is a \int -shaped sub-linear dependence, where background count rate and dead-time saturation dominate on opposite sides of the power range. However, we found that some detectors exhibit an S-shaped response where the slope gets supralinear in the middle. Supralinearity has been reported for silicon photodiodes for strong classical illumination [27–29], but current SPAD models and measurements do not predict any such phenomenon. For SNSPDs, supralinear behavior has been observed for very high rates (≥ 10 Mcps) due to AC detector coupling [30] and for short optical pulses (mean photon number ≥ 0.1) as a result of two-photon absorption [31]. However, no observation of supralinearity of SNSPDs has been reported under continuous illumination with the detection rate below 1 Mcps.

The particular detection imperfections are specific to

SPADs and their quenching circuits [23, 24], or SNSPDs [22, 25, 26] due to their different operational principles. There is a great number of results in modelling the response of a SPAD with the goal of including all the relevant factors [32–36]. Their accuracy has been limited so far and many counter-examples exist for which the measured SPAD response differs from the theoretical model. Consequently, determining the nonlinearity of the SPAD response and finding the optimum detection rate to access the minimum achievable deviation from the ideal linear behavior represents a significant challenge. This issue is even more pronounced for SNSPDs due to the lack of a precise theoretical model taking into account all physical processes [31]. A semi-empirical model was proposed and tested with the accuracy 10^{-2} [37, 38]. Detector tomography based on probing with precisely calibrated signals was suggested to thoroughly characterize a detector and obtain the corresponding positive-operator-valued measure [38–46]. However, if the tomography does not include memory effects, the results can be compromised [47]. The approach presented in the rest of the paper does not rely on a theoretical model or detector tomography. Instead, we focus on a direct measurement of the detector nonlinearity as a function of the detection rate.

B. Nonlinearity characterization

The nonlinearity of various photodetectors, mainly photodiodes, have been explored in great depth using relative and absolute measurement methods [48]. Relative methods require a calibrated reference detector, calibrated attenuators, or time-resolved probe signals and detection. Absolute measurements, which are generally preferred, are based on a superposition method where the response of the detector is evaluated separately for two signals and their total [27, 49–54]. The individual signals have to be incoherent to prevent optical interference. Often two independent optical sources are used for this reason [54], preferably exhibiting short coherence lengths [53]. Optionally, the two signals are derived from the same source and superimposed in a slightly misaligned interferometer [51, 52]. Direct absolute measurement of nonlinearity of a SPAD under continuous illumination was reported by Kauten et al., and no statistically significant deviation from the standard model (Eq. (2) below) was found [54]. We follow a single-source approach to directly characterize major single-photon technologies, namely passively and actively quenched SPADs, and SNSPDs for various values of bias current. Our measurements reveal deviations from standard models, as well as anomalous supralinearity.

II. DIRECT NONLINEARITY MEASUREMENT

We employ the absolute measurement strategy based on the single-source two-beam superposition method.

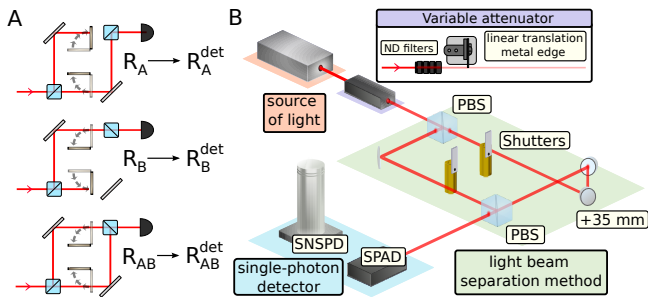


FIG. 2. The single-source two-beam method for absolute measurement of nonlinearity consisting of three measurements of the detection rate (A) and the simplified experimental scheme of the method (B).

For a constant intensity level of the optical source, a series of three measurements is performed, see Fig. 2(A). The beam is split into two paths A and B that can be individually blocked. The detection rates R_A^{det} and R_B^{det} are recorded for each path, and R_{AB}^{det} is acquired with both paths open. The nonlinearity is defined as a deviation from the ideal linear response,

$$\Delta = \frac{R_A^{\text{det}} + R_B^{\text{det}}}{R_{AB}^{\text{det}}} - 1. \quad (1)$$

The splitting ratio $R_A^{\text{det}} : R_B^{\text{det}}$ is chosen to be 50:50. For the ultimate nonlinearity characterization, all splitting ratios would need to be measured, but without calibration, the 50:50 splitting is the only one that can be set with certainty, as $R_A^{\text{det}} = R_B^{\text{det}}$. Furthermore, it harnesses the method's invariance—a 10% deviation from the 50% splitting leads to a $\leq 4\%$ relative error in Δ . This is in contrast to using a 3dB attenuator, where a 1% error in its transmission can change Δ by an order of magnitude (see the discussion in the Appendix D).

The experimental setup is shown in Fig. 2(B). A stabilized super-luminescence diode is the source, with the central wavelength 810 nm and the spectral width exceeding 20 nm. The signal is attenuated to scan the input power over the full dynamic range. To avoid phase interference, the beam is split and joined using polarization beam splitters (PBS), with a 35-mm path difference that is several orders of magnitude larger than the coherence length. The output of the Mach-Zehnder is coupled into a single-mode optical fiber connected to the active area of the single-photon detector under test. The fiber coupling guarantees the same spatial profile of the signals at the detector, but it can decrease the overall stability. Therefore, extra effort was made to reach 10^{-5} power stability of the setup including the coupling stages (see Appendix B).

In the case of SNSPD measurements, the source spectrum was filtered to 12 nm around 800 nm, for which the detector is optimized. The reduced spectral width corresponds to a coherence length shorter than 30 μm . The coupling fiber was equipped with a diagonal polarizer and

a polarization controller to set the optimal polarization for maximization of the SNSPD efficiency. In this case, the incoherence relied solely on the Mach-Zehnder path difference.

The acquisition time of each individual rate measurement was set to 20 s, amounting to 1 min per triplet. The complete characterization of a single detector typically took 20 hours with each measurement repeated 30 times for 40 different rate levels. The precision was found to be limited mostly by fundamental Poissonian variance (see Appendix C).

We measured three actively quenched SPADs (SPAD-1–3), a passively quenched SPAD (SPAD-P), and an SNSPD for various values of bias current. The output of the detector under test is processed by a custom FPGA-based counter with a 2.2 ns pulse-pair resolution that is well below the dead time of any detector. For technical information, see Appendix A.

III. RESULTS AND DISCUSSION

A. Single-photon avalanche diodes

Figure 3 shows the measured nonlinearity as a function of the detection rate R_{AB}^{det} for various SPADs. The typical log-log plot of the SPAD nonlinearity Δ is V-shaped due to dark counts (left slope) and dead time saturation (right slope). The nonlinearity reaches its minimum value ($10^{-3} - 10^{-2}$) for detection rates between 10^4 and 10^5 cps.

The established model of the detection rate R^{det} takes into account the dark count rate R_0 and the non-paralyzable dead time τ [36, 54], reading

$$R^{\text{det}} = f(R) = \frac{R + R_0}{1 + (R + R_0)\tau}, \quad (2)$$

where R is the incident rate. The nonlinearity is measured in a balanced configuration, so that the incident rates are $R_A = R_B = R_{AB}/2$. If we substitute the detector model $R^{\text{det}} = f(R)$ given in Eq. (2), we obtain the detection rates $R_A^{\text{det}} = R_B^{\text{det}} = f(f^{-1}(R_{AB}^{\text{det}})/2)$. The expected nonlinearity as a function of detection rate is

$$\Delta(R_{AB}^{\text{det}}) = \frac{2f(\frac{1}{2}f^{-1}(R_{AB}^{\text{det}}))}{R_{AB}^{\text{det}}} - 1. \quad (3)$$

The parameters of this model are the dark count rate R_0 and dead time τ . More elaborate models of actively quenched SPADs are discussed in Appendix F, although none provide a better fit than (2).

The data were fit with Eq. (3) in Fig. 3, and they are in significant disagreement with the model, affirming the need for direct nonlinearity measurement. The most prominent feature is the supralinear behavior ($\Delta < 0$) in Fig. 3(C), which is a hitherto unreported phenomenon for SPADs. In fact, all actively quenched SPAD-1–3 exhibit systematically lower nonlinearities than expected in their

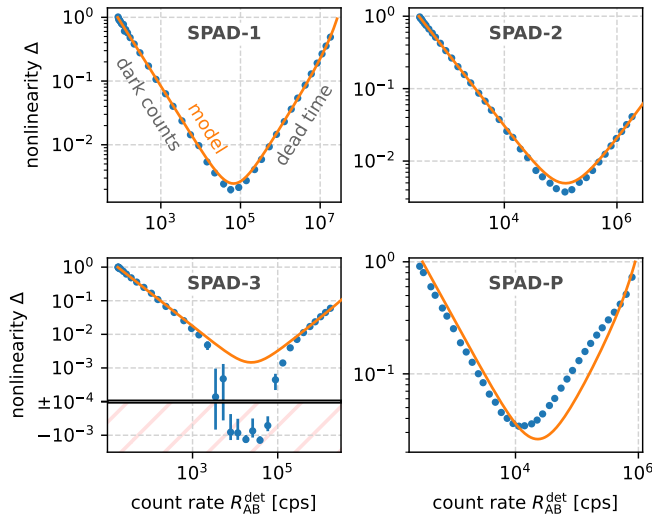


FIG. 3. Nonlinear response of the tested SPADs. Solid line represents the theoretical model (3). Each point was measured 30 times and the error bars show the corresponding standard error of the mean.

	SPAD-1	SPAD-2	SPAD-3	SPAD-P
τ_R [ns]	29.5(5)	47.0(5)	56.6(4)	517(6)
τ_{fit} [ns]	36.7(1)	40.2(4)	61(1)	1130(20)

TABLE I. Comparison of recovery times τ_R that were measured directly using time-resolved detection techniques [36], and the dead time values τ_{fit} that were the best fit of the model (2).

minima. Additionally, the fit parameters R_0, τ do not agree with values that were obtained from independent time-resolved measurements.

A comparison of dead times and directly observed recovery times is given in Table I. For actively quenched detectors (SPAD-1–3), the measured recovery time τ_R also includes a brief detector reset time, and so must always be $\tau_R \geq \tau$ [55]. Reset effects like twilight pulsing could therefore explain the difference for SPAD-2, but not for the other detectors SPAD-1 and SPAD-3 [36]. SPAD-P is passively quenched and so the recovery and dead time values differ significantly. Such detectors exhibit gradual efficiency recovery after each detection, which would require a complex empirical model. As shown in Appendix F, no other few-parameter models offer a better fit than (2).

Because not all systematic errors can be seen in Fig. 3, we evaluated the χ^2 with the highest p -value being $p_{\text{SPAD-2}} \sim 10^{-70}$. It means that under the assumption that the model (2) is valid and only the statistical error takes effect, the probability of obtaining the measured data or any worse data would be equal to the p -value. This means that the model (2) already deviates from the measurement with high statistical significance for 20 s integration times. Additionally, we applied standard rate

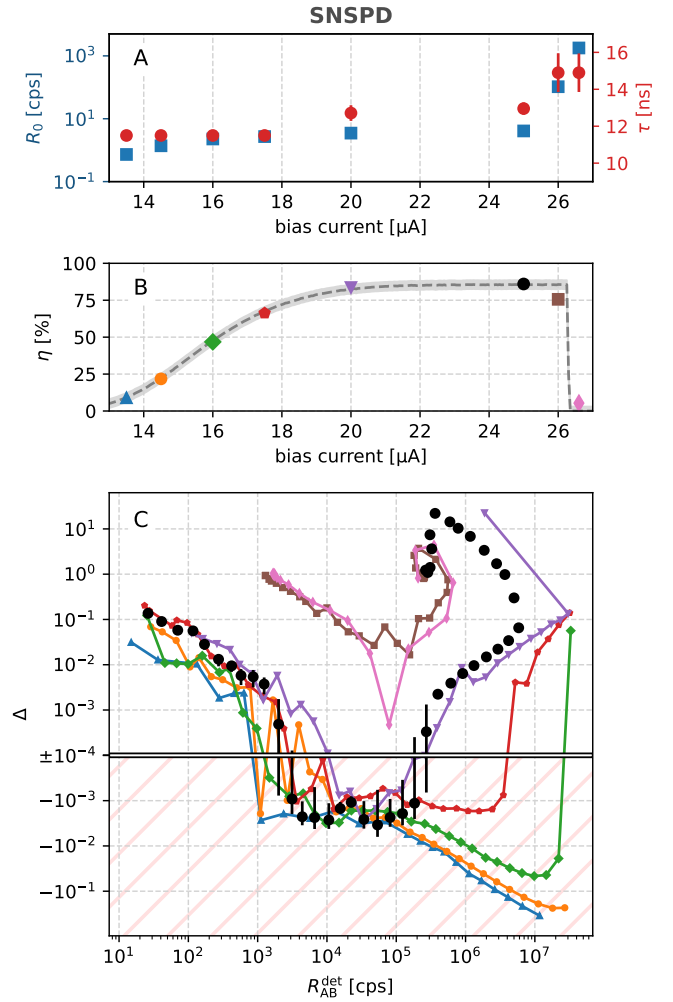


FIG. 4. (A) Dark counts R_0 , dead time τ and (B) detection efficiency η as a function of bias current. Dashed line is the manufacturer's specification. (C) the measured nonlinearity of the SNSPD for the values of bias current given by the respective markers in (B).

corrections on the data (inversion of (2)) to evaluate any residual nonlinearity, which reveals significant mismatch even for $R_{\text{AB}}^{\text{det}} \gtrsim 10^6$ cps. A detailed statistical analysis can be found in Appendix F.

We have also tested more elaborate response models such as Ref. [36] (including dead time, afterpulses, and twilight pulses), and a combination of paralyzable and non-paralyzable dead time [56–61] developed originally for Geiger–Müller detectors. None of these can reproduce the measured results or explain supralinearity, which is shown in Appendix F.

Current evidence shows that SPADs exhibit neither constant dark counts [62], nor constant recovery time (dead time + reset time) [36]. This means that state-of-the-art models are insufficient, leaving the experimentalist with two options: 1. a detailed characterization of the SPAD involving time-resolved measurements and circuit analysis. 2. direct nonlinearity measurement.

B. Superconducting nanowire single-photon detectors

Figure 4 shows nonlinearity of the SNSPD with respect to the bias current. The temperature of the detector was kept at 2.7 K. Subfig. 4(A) shows the dependence of dead time and dark counts on the bias. The property affected the most is detection efficiency, shown in subfig. 4(B). The detection efficiencies were calculated relatively to the manufacturer’s specification of $86 \pm 3\%$ for 25 μA . Subfig. 4(C) shows the measured nonlinearity Δ as a function of the total detected rate $R_{\text{AB}}^{\text{det}}$. Each data set corresponds to a different bias current, where the plot markers match the respective points in subfig. 4(B).

The nonlinearity of the SNSPD is a combination of several phenomena. For lower rates, the effect of dark counts is easily recognizable. Around 10^4 cps, all subcritical regimes ($I_{\text{bias}} \leq 25 \mu\text{A}$) begin to exhibit supralinearity ($\Delta < 0$). For higher count rates, two scenarios are observed. Bias currents corresponding to the efficiency plateau (20–25 μA) lead to dead time saturation, while lower biases maintain the supralinearity. Finally, for $R_{\text{AB}}^{\text{det}} > 10^6$ cps, latching rapidly increases for all but the lowest biases. This introduces strong saturation and eventually results in an inverse detection response, where count rate decreases with increasing illumination.

Let us address the supralinear behavior, linked previously to two effects. With decreasing bias current, two-photon and higher-order detection efficiencies rise as indicated by detector tomography [38]. So far, the two-photon absorption of SNSPDs was observed for ultra-short optical pulses in picosecond regime with mean photon numbers ≥ 0.1 [31]. Under continuous illumination, the multi-photon absorption becomes challenging to model due to hotspot relaxation dynamics [31]. The second factor is the AC coupling of the readout circuit—the settling of the bias current after each detection results in rate-dependent efficiency. The supralinear behavior due to the AC coupling was observed only for very high rates ≥ 10 Mcps [30]. Our results represent the first observation of the SNSPDs supralinearity under continuous illumination with the detection rates as low as 10^3 cps.

IV. CONCLUSION

In summary, we designed and realized a direct measurement of single-photon detection absolute nonlinearity with high accuracy over several orders of magnitude of light intensity. We performed the measurement for SPAD and SNSPD detectors. The measurement technique does not require a calibrated reference detector or time-resolved detection. Due to the method’s robustness, the nonlinearity is not affected by technical issues, but rather reflects the detector properties.

For all SPADs, we found significant disagreement of established theoretical models with the measured data. We also discovered anomalous supralinear behavior of a

SPAD. This phenomenon has been neither predicted nor observed yet. For the SNSPD, we performed its detailed nonlinearity analysis over 7 orders of magnitude of incident illumination and the full range of relevant values of bias current, which goes beyond any SNSPD characterization reported so far. We detected SNSPD supralinearity under continuous illumination at unprecedentedly low detection rates down to 10^3 cps, which has not been observed before. The results for both SPADs and SNSPDs show that nonlinearity in single-photon detection is a complex mixture of non-trivial phenomena which have so far eluded accurate theoretical description.

Our findings can be applied to radiometric, spectroscopic, imaging, and optical communication methods that rely on precise assessment of illumination or transmission levels. We have shown that correcting for nonlinear aspects based on state-of-the-art response models is generally not sufficient, and so direct measurement of nonlinearity becomes a necessity. Accurate detector calibration is particularly critical for measuring photon statistics and reaching the quantum advantage in quantum metrology. The presented results open the way for ultra-precise identification and mitigation of nonlinear effects in single-photon detectors.

V. ACKNOWLEDGMENTS

We acknowledge the funding from the Czech Science Foundation, project 21-18545S; MEYS and European Union’s Horizon 2020 (2014–2020) research and innovation framework programme (project HYPER-U-P-S, No. 8C18002); Project HYPER-U-P-S as part of the QuantERA ERANET Cofund in Quantum Technologies implemented within the European Union’s Horizon 2020 Programme; and Palacký University projects IGA-PrF-2020-009, IGA-PrF-2021-006, IGA-PrF-2022-005.

a. Conflict of interest statement. The custom-made counter used in the presented measurements is commercially available and sold by the Palacký University. M.J. is one of the developers and thus eligible for a percentage of the income. However, the presented measurements are not affected by the choice of the counter, as the necessary parameters can be met by other devices available on the market. All other authors declare they have no competing interests.

b. Data availability statement. Data underlying the results presented in this paper are available in Ref. [63].

Appendix A: Experimental setup

Figure 5 depicts the experimental setup for absolute measurement of nonlinearity using the single-source two-beam superposition method. The light source is a temperature-stabilized super-luminescence diode (QPhotonics QSDM-810-2) in constant current mode with the

central wavelength of 810 nm and the spectral width exceeding 20 nm. Angled physical contacts (APC) between optical fibers reduce back-reflections approximately by 60 dB and improve the stability of the source. Attenuation by several orders of magnitude is needed to generate an optical signal in the dynamic range of the tested detector. For this purpose, the optical beam is strongly attenuated by a series of neutral density (ND) filters (Thorlabs NE530, NE520, NE513, and NE504) down to $\sim 10^7$ counts per second. Continuous adjustment is realized by a metal edge fixed to a linear translation motorized stage (LTME, Newport MFA-CC) driven by a motion controller (SMC-100CC). The moving edge along with single-mode fiber coupling serves as variable attenuation.

Since the splitting ratio of the interferometer is sensitive to input polarization, the input beam is well polarized and coupled in the slow axis of a polarization-maintaining fiber. The unbalanced Mach-Zehnder interferometer consists of two polarizing beam splitters (PBS) with extinction ratio $T_P : T_S > 1000 : 1$. The Mach-Zehnder setup is used to split the attenuated beam into two spatially separated beams that can be individually blocked and superimposed again at the output. The combination of perpendicular polarizations and the path difference $l = 35.4$ mm between the individual arms ensure incoherent mixing at the second polarization beam splitter. Mechanical blocking of the two optical signals is done by compact home-made optical shutters using a digital RC servo (Savox SH-0262MG). Thin (0.5 mm) metal flag with dimensions 15×70 mm attached to the servo shaft blocks the collimated Gaussian beam that has a radius $w_0 = 1.03$ mm. To perform the operation of opening or blocking the beam, it is necessary to turn the servo by 15° with a total latency of 50 ms. The RC servo is controlled by a pulse-width modulation signal generated by Arduino Uno with a microprocessor AT-mega328. For more information about the employed shutters, see [64]. After the second PBS, the output light is fed into a single-mode fiber and coupled to the tested detector. Stray light is eliminated by a cut-off filter (Semrock BLP01-635R-25).

We investigated the response of five single-photon detectors: actively (SPAD-1–3) and passively quenched (SPAD-P) thick-junction silicon single-photon avalanche diodes (SPADs), and a NbTiN superconducting nanowire single-photon detector (SNSPD) with AC readout and room-temperature amplifier. Namely, SPAD-1 – Excelitas SPCM-AQRH CD3432H, SPAD-2 – Perkin Elmer SPCM-AQ4C module s.n. 167, SPAD-3 – Laser Components COUNT-20C-FC D4967, SPAD-P – ID Quantique ID120 s.n. 1518006, and SNSPD – Single Quantum Eos CS SNSPD system s.n. SQ071. The detectors differ in many technical parameters and physical effects such as active area, photon detection efficiency, dark count rate, dead time, and afterpulsing probability. The manufacturer’s specifications are shown in Table II. The detector SPAD-P (ID Quantique ID120) differs from SPAD-1–3 not only by the passive quenching mechanism, but also by being a free-space module with tunable temperature

and bias voltage. All measurements were done at the temperature -40°C and bias voltage 180 V.

The SNSPD possesses a limited spectral region of the maximum efficiency. For this reason, the wide emission of SLED was reduced using a 12 nm band-pass interference filter (Semrock FF01-800/12-25). Furthermore, the SNSPD is naturally sensitive to polarization due to its nanowire structure. The optical beams of the unbalanced Mach-Zehnder interferometer have orthogonal H/V polarizations, so it is necessary to add a diagonally oriented linear polarizer (LP) at the output to make them indistinguishable for the detector. A fiber polarization controller (FPC) is used to optimize the detection efficiency with respect to polarization.

Electric output signals from the tested detectors were processed by an electronic counter. The most critical parameter is its pulse-pair resolution, which has to be better than the recovery time of all tested detectors. Initially, we were using a commercial 100 MHz counter (ORTEC 974C), which was used to measure the SPADs. Later, we developed an FPGA-based 230 MHz counter with a 2.2 ns pulse-pair resolution and digitally tunable threshold voltages (QOLO Countex [65]). This counter was used to perform measurements on the SNSPD, as well as additional measurements on SPAD-1 and SPAD-3. Detectors SPAD-1 and SPAD-3 were measured using both counters with the same results.

	A [μm]	η [%]	R_0 [cps]	τ [ns]	p_a [%]
SPAD-1	180	50	<100	28.7	0.1
SPAD-2	180	47	<500	50	0.3
SPAD-3	100	57	<20	55	0.31
SPAD-P	500	80	200	1000	negligible
SNSPD	–	86	≤ 10	≤ 10	none

TABLE II. Manufacturer specifications for tested detectors. Parameters shown: active area diameter A , photon detection efficiency η , dark count rate R_0 , dead time τ , and afterpulsing probability p_a .

Appendix B: Stability of the source and measurement setup

Generally, intensity fluctuations of the light source can affect the measurement accuracy. We investigated the stability of the SLED and also the intensity stability at the output of the setup. We performed a long-term measurement of optical intensity and evaluated the Allan deviation [66] to determine the integration time T for which the measurement is least affected by intensity fluctuations. Figure 6 shows the relative Allan deviation σ_{Allan} as a function of the integration time T . The deviation is better than 10^{-5} for integration times from 10 s to 10^3 s. For the nonlinearity measurement setup, optimal integration times are shifted toward shorter times and the minimum relative Allan deviation gets worse, but still

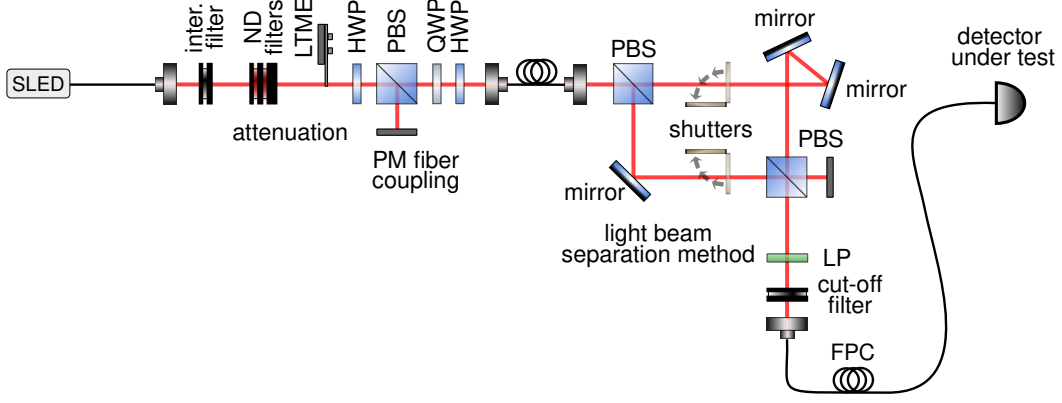


FIG. 5. Experimental setup of the single-source two-beam superposition method for absolute nonlinearity measurement: the scheme includes preparation of a stabilized and attenuated optical signal, its polarization control, beam separation and switching, and detector under test.

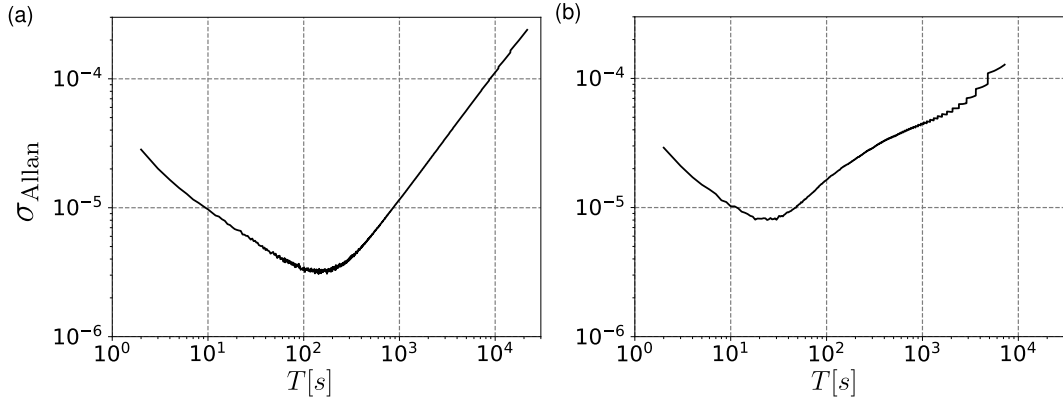


FIG. 6. Optical intensity fluctuations represented by the relative Allan deviation. Shown are: (a) temperature-stabilized super-luminescence diode (QPhotonics QSDM-810-2) in constant current mode, and (b) signal from the same source transmitted through the experimental setup for nonlinearity measurement.

below 10^{-4} for integration times up to 6×10^3 s. The raw data and their processing are available on GitHub [63].

Appendix C: Measurement uncertainty

1. Shot noise limitation

We performed an analysis of nonlinearity measurement uncertainty $\sigma(\Delta)$ to find its ultimate physical limits and find out whether the data approach the fundamental nonlinearity resolution. The statistical uncertainty was calculated for the case of a balanced experimental setup $R_A^{\text{det}} = R_B^{\text{det}}$, measurement time $T = 20$ s for each rate, and $N = 30$ repeated measurements.

The fundamental limit is represented by the shot noise of the Poisson counting process, where the measured number of events ($R^{\text{det}}T$) exhibits variance equal to the mean value. This implies the standard deviation of the

detection rate $\sigma(R^{\text{det}}) = \sqrt{R^{\text{det}}/T}$. If we introduce this standard deviation to each detection rate in the nonlinearity formula

$$\Delta = \frac{R_A^{\text{det}} + R_B^{\text{det}}}{R_{AB}^{\text{det}}} - 1, \quad (\text{C1})$$

through standard error propagation $\sigma^2(\Delta) = \sum_i [\sigma(R_i^{\text{det}}) \times \partial\Delta/\partial R_i^{\text{det}}]^2$, we obtain the standard deviation

$$\sigma(\Delta) = \sqrt{\frac{(1+\Delta)(2+\Delta)}{R_{AB}^{\text{det}}T}} \approx \sqrt{\frac{2}{R_{AB}^{\text{det}}T}}. \quad (\text{C2})$$

The measured nonlinearity $\bar{\Delta}$ is averaged from N measurements, so the standard deviation of the result is

$$\sigma(\bar{\Delta}) = \sigma(\Delta)/\sqrt{N}. \quad (\text{C3})$$

This limit is compared to the experimental values in Fig. 7. The measured standard errors of the nonlinearity

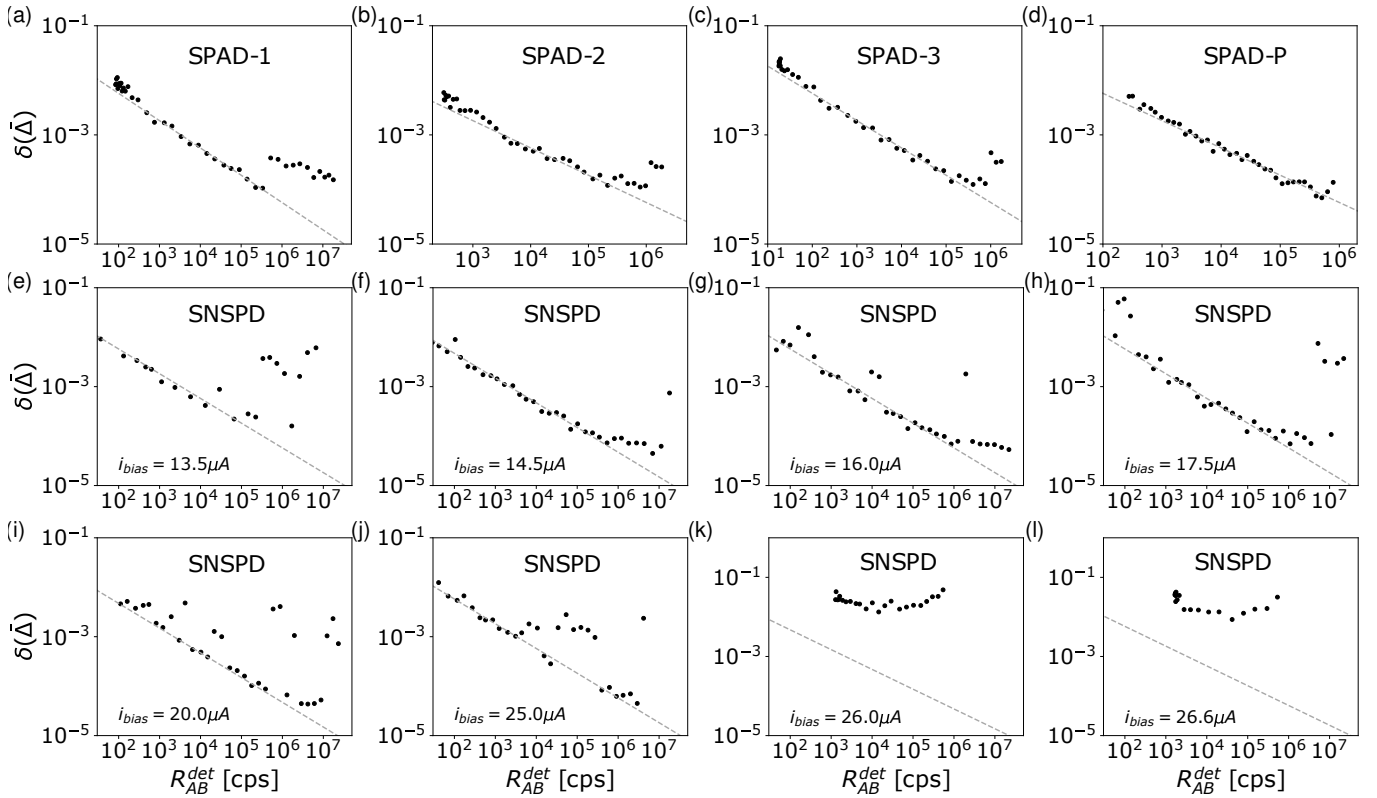


FIG. 7. The nonlinearity measurement standard error $\sigma(\overline{\Delta})$ of tested detectors (a) SPAD-1, (b) SPAD-2, (c) SPAD-3, (d) SPAD-P and (e-f) SNSPD as a function of detection rate R_{AB}^{det} . Subplots (e-f) show $\sigma(\overline{\Delta})$ of an SNSPD with respect to the bias current. The measured standard errors are plotted as black dots, and the lower bound on the standard deviation is represented as a grey dashed line.

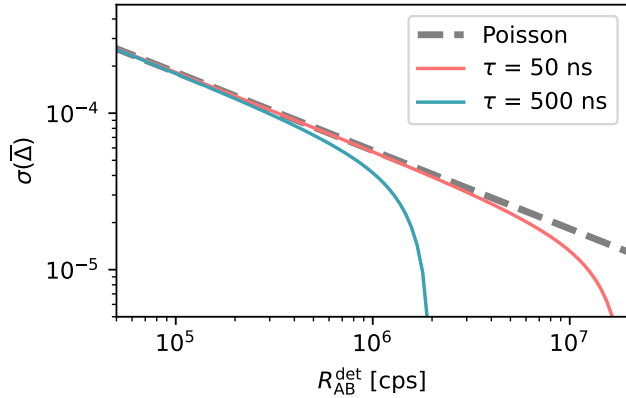


FIG. 8. The effect of dead-time saturation on the fundamental limit of uncertainty resolution. The integration time is $T = 20$ s and the number of measurements $N = 30$.

for SPADs meet their lower bound 10^{-4} for rates higher than 2×10^5 cps (Fig. 7(a-d)). For higher rates, excess noise limits the measurement uncertainty; it nevertheless remains below $\sigma(\overline{\Delta}) < 10^{-3}$. In this region, the mean nonlinearity value is larger than the uncertainty by at least one order of magnitude. Subfigures (e-l) show the

nonlinearity measurement uncertainty of the SNSPD for several different values of bias current. Latching rapidly increases for bias current $I_{\text{bias}} > 25 \mu\text{A}$ and brings extra uncertainty to the measurement (Fig. 3(k-l)).

The shot noise limit is well applicable to Poisson count rates. However, dead-time saturation will further affect the measurement, because the measured count rates become sub-Poissonian as they approach the limit $R^{\text{det}} \rightarrow 1/\tau_{\text{NP}}$. Because the standard deviation of accumulated counts is complicated to calculate analytically [36], we are going to assume a sufficiently long integration time so that the number of accumulated counts is large: $\langle n \rangle = R^{\text{det}}T \gg 1$. This is a reasonable assumption for high rates, where saturation occurs. Then, we can make the following derivation.

Upon measuring n detections during a time T , we obtain the average time between detections, $\overline{\Delta t} = T/n$. Because each realization of Δt is independent, the average time $\overline{\Delta t}$ is normally distributed with a standard deviation $\sigma(\overline{\Delta t}) = \sigma(\Delta t)/\sqrt{n}$ according to the central limit theorem. We assume Δt to be a dead time τ_{NP} plus an exponentially distributed delay with a rate parameter λ , which makes $\langle \Delta t \rangle = \tau_{\text{NP}} + 1/\lambda$ and $\sigma(\Delta t) = 1/\lambda$. Because $n \gg 1$, the standard deviation is small relative to the mean; $\sigma(\overline{\Delta t}) \ll \langle \overline{\Delta t} \rangle$. As a result, the mean rate

$R^{\text{det}} = 1/\overline{\Delta t}$ is also normally distributed and the standard deviation is scaled based on the slope around the mean value,

$$\sigma(R^{\text{det}}) = \left| \frac{\partial R^{\text{det}}}{\partial \overline{\Delta t}} \right| \sigma(\overline{\Delta t}) = (R^{\text{det}})^2 \sigma(\overline{\Delta t}). \quad (\text{C4})$$

Due to the large number of detections, on the right side we can simplify $\overline{\Delta t} \approx \langle \Delta t \rangle \approx 1/R^{\text{det}}$, so

$$\sigma(R^{\text{det}}) = (1 - \tau_{\text{NP}} R^{\text{det}}) \sqrt{R^{\text{det}}/T}. \quad (\text{C5})$$

The resulting sub-Poissonian bounds are shown in Fig. 8 for two dead time values to illustrate the cases of an actively and passively quenched detectors. The bounds do not make a difference within the data range of Fig. 7.

2. Optimal measurement times

Here we address the optimal allocation of measurement time to minimize the uncertainty. Given the overall measurement time T_O per one sample of Δ , there exists an optimal distribution between measuring R_A^{det} , R_B^{det} , and $R_{\text{AB}}^{\text{det}}$. Assuming a balanced splitting $R_A^{\text{det}} \approx R_B^{\text{det}}$, the minimum uncertainty of Δ is reached for

$$T_{\text{AB}} = \frac{T_O}{1 + \sqrt{2/(1 + \Delta)}}, \quad (\text{C6})$$

$$T_A = T_B = \frac{1}{2}(T_O - T_{\text{AB}}). \quad (\text{C7})$$

In the regime where $|\Delta| \ll 1$, the approximate ratios are $T_A : T_B : T_{\text{AB}} = 0.3 : 0.3 : 0.4$. The assumption we made on the way is that the measurement time is long enough so that all the accumulated counts C_i ($i = A, B, \text{AB}$) are approximately normally distributed. This holds if $\langle C_i \rangle = R_i^{\text{det}} T_i \gg 1$.

Appendix D: Two-beam method compared to an attenuator

Here we illustrate the advantage of the two-beam method compared to single-beam measurements. An analogous way of characterizing nonlinearity is comparing the detection rates of two intensity levels by employing an attenuator of power transmittance η . The nonlinearity Δ essentially tests two quantities that should be equal if the detector was linear; $R_A^{\text{det}} + R_B^{\text{det}} \stackrel{?}{=} R_{\text{AB}}^{\text{det}}$. With an attenuator, we can only measure the transmitted power R_η^{det} and total power R_1^{det} , whereas the lost power $R_{1-\eta}^{\text{det}}$ is inaccessible. We can, however, analogously test $R_{1-\eta}^{\text{det}} \stackrel{?}{=} \frac{1-\eta}{\eta} R_\eta^{\text{det}}$. Thus, we construct nonlinearity

$$\Delta^{\text{att}} = \frac{R_\eta^{\text{det}} + \frac{1-\eta}{\eta} R_\eta^{\text{det}}}{R^{\text{det}}} - 1 = \frac{1}{\eta} \frac{R_\eta^{\text{det}}}{R^{\text{det}}} - 1. \quad (\text{D1})$$

For $\eta = 1/2$, this is equal to nonlinearity Δ (1).

Let us examine a scenario where we attempt to measure nonlinearity for a balanced scheme, but there is a slight error in calibration,

$$\eta = 0.5 + \delta\eta. \quad (\text{D2})$$

Because the value of nonlinearity may span many orders of magnitude, let us examine its *relative* error, meaning the difference proportional to the ideal value of Δ for $\eta = 0.5$:

$$\delta\Delta = \left| \frac{\Delta(0.5 + \delta\eta) - \Delta(0.5)}{\Delta(0.5)} \right|. \quad (\text{D3})$$

This will generally depend on the model of the detector and the incident rate, so let us illustrate the basic behavior for a simple non-paralyzing model with background R_0 and dead time τ

$$R_\eta^{\text{det}} := R^{\text{det}}(\eta R) = \frac{1}{\frac{1}{\eta R + R_0} + \tau}. \quad (\text{D4})$$

The nonlinearity for the two-beam measurement is then

$$\Delta(\eta) = \frac{R_\eta^{\text{det}} + R_{1-\eta}^{\text{det}}}{R_1^{\text{det}}} - 1, \quad (\text{D5})$$

while for the attenuator, an unknown error manifests only in the measured intensity,

$$\Delta^{\text{att}}(\eta) = \frac{1}{0.5} \frac{R_\eta^{\text{det}}}{R_1^{\text{det}}} - 1. \quad (\text{D6})$$

Apart from η , these quantities depend on R , R_0 , and τ . When examining the error, we look for the maximum over all incident rates R . Thus, we obtain the maximum relative error (for both nonlinearities)

$$\delta\Delta_{\text{max}}(\delta\eta) = \max_R \left| \frac{\Delta(0.5 + \delta\eta)}{\Delta(0.5)} - 1 \right|. \quad (\text{D7})$$

Now, let us assume a small error in calibration $\delta\eta \ll 1$, so we can consider polynomial contributions of $\delta\eta$. Let us also examine the quantities for a certain realistic range of parameters,

$$0 < R_0 < 10^3 \text{ cps}, \quad (\text{D8})$$

$$0 < \tau < 10^{-6} \text{ s}. \quad (\text{D9})$$

For $\delta\Delta_{\text{max}}^{\text{att}}$, we make certain approximations, chiefly $R_0\tau \ll 1$, that yield the maximal rate $R \approx \sqrt{2R_0/\tau}$ and

$$\delta\Delta_{\text{max}}^{\text{att}} \approx \sqrt{\frac{2}{R_0\tau}} \times \delta\eta. \quad (\text{D10})$$

On the other hand, the two-beam nonlinearity error scales more favorably, and with a constant factor,

$$\delta\Delta_{\text{max}} \approx 4 \times \delta\eta^2. \quad (\text{D11})$$

In practical terms, for a 1% deviation in beam splitter transmittance, $\delta\eta = 0.01$, the value of nonlinearity measured by the two-beam method will change by $\delta\Delta \lesssim 0.04\%$ for any realistic dead time and dark counts.

If the same 1% error is applied to an attenuator, the error depends on the detector parameters. For an extreme case of $R_0 = 10^3$ cps and $\tau = 1 \mu\text{s}$, the error is $\delta\Delta^{\text{att}} \lesssim 44\%$, whereas for values corresponding more with modern SPADs, $R_0 = 50$ cps and $\tau = 30$ ns, the value can change drastically by $\delta\Delta^{\text{att}} \lesssim 1200\%$.

By accessing the complementary optical power, the two-beam nonlinearity offers a much more reliable measurement. The dependence on the splitting ratio is quite weak, with the value of Δ changing by $\lesssim 15\%$ within the range $\eta \in (0.3, 0.7)$ relative to $\eta = 0.5$. Furthermore, the balanced splitting ratio is the only one that can be calibrated with arbitrary precision, so it easily becomes the most suitable measurement setting to use, as it represents the nonlinear properties of the detector much more than any technical parameters of the measurement.

Appendix E: Repeatability of the measurement

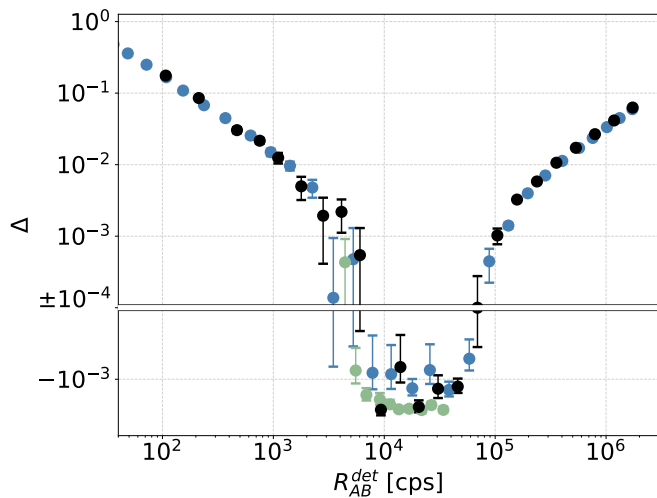


FIG. 9. The repeatability of the nonlinearity measurement of the detector SPAD-3 throughout the years. The nonlinearity Δ is a function of the detection rate R_{AB}^{det} , shown at different dates: black – February 2021, green – January 2016, and blue – November 2014.

In 2014 we built the experimental setup for absolute measurement of nonlinearity to characterize the detector response and since then, we have performed nonlinearity measurements repeatedly. As an example representing the consistency of the results obtained from the presented method, we chose the actively quenched SPAD from Laser Components (SPAD-3). This detector exhibits anomalous supralinear behavior ($\Delta < 0$) for all measurements. Figure 9 shows individual nonlinearity measurements separated by years during which the

detector was used in many other experimental setups. The first measurement of nonlinearity was performed in November 2014 using the Ortec counter (Fig. 9 – blue). In January 2016, we repeated the measurement—again using the Ortec counter—in order to confirm the supralinear response of the tested detector (Fig. 9 – green). This was the most accurate measurement, with acquisition time 120 s for each individual rate measurement, repeated 20 times. The last measurement was performed in February 2021 using the Countex counter (Fig. 9 – black). Throughout the years, we have obtained consistent results.

Appendix F: Theoretical models of the SPAD response function

1. Correcting the data for dead time and background

There have been many SPAD response models proposed that model saturation effects and noise [32–36, 55, 62, 67]. The model used to fit the presented results considers a non-paralyzable dead time τ_{NP} , dark count rate R_0 , and neglects afterpulsing. The rate of detection events as a function of the incident rate R then follows a standard formula

$$f_{\text{NP}}(R) = \frac{R + R_0}{1 + (R + R_0)\tau_{\text{NP}}}. \quad (\text{F1})$$

In Fig. 10, we illustrate the effects of dead time and dark counts, when this model is applied to nonlinearity (1). The left slope represents the background noise characterized by dark counts and the right slope represents dead time saturation. Other theoretical models shown below yield similarly V-shaped nonlinearity Δ with analogous scaling.

To correct for nonlinearities under this model, one can apply the formula

$$R_i^{\text{corr}} = \frac{R_i^{\text{det}}}{1 - R_i^{\text{det}}\tau_{\text{NP}}} - R_0 \quad (\text{F2})$$

with $i \in \{A, B, AB\}$ to the measured detection rates. Fig. 11 shows the nonlinearity values calculated from corrected rates. The same data as presented in the main text are used, and the values of R_0 and τ_{NP} are taken from the least-squares fits (see Fig. 12 and Table III below).

If the model (F1) holds, then the corrected nonlinearity should be close to zero. However, due to the Poissonian uncertainty (C5) and the nonlinear nature of the formula (C1), there is a nonzero bias (solid line in Fig. 11). The exact probability distribution of Δ^{corr} needs to be computed numerically for $R_{AB}^{\text{corr}} < 10^2$ cps, because a normal approximation no longer holds [63].

Like in the main text, each point represents the average from 30 measurements. To test the compatibility of the corrected data and the model (F1), we test both

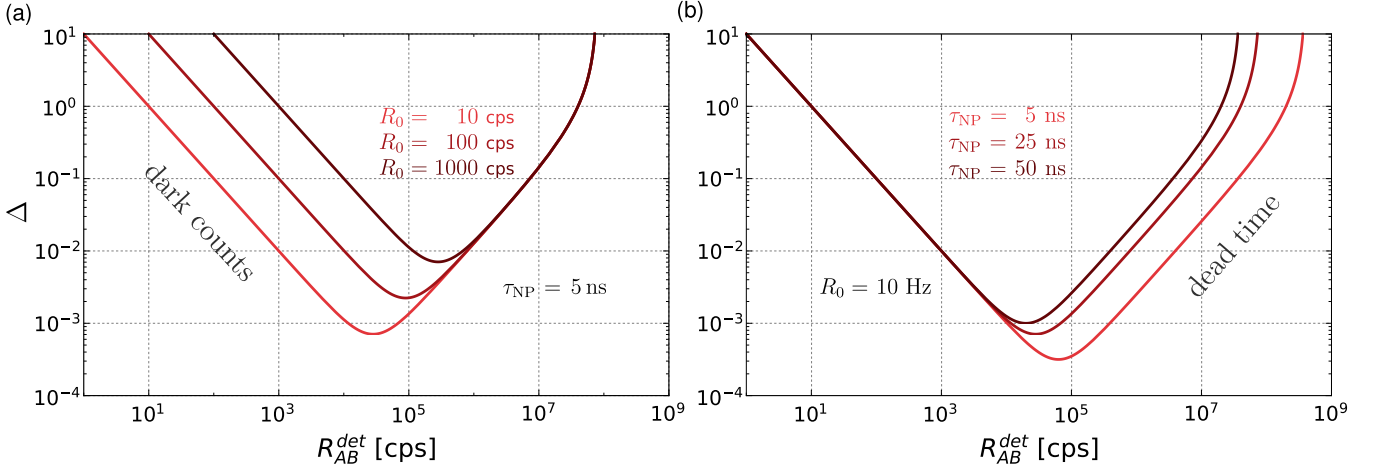


FIG. 10. Nonlinearity Δ as a function of the detection rate R_{AB}^{det} for (a) a several different values of dark counts: $R_0 = 10, 100, 1000$ cps ($\tau = \text{const.}$) and (b) dead time: $\tau = 5, 25, 50$ ns ($R_0 = \text{const.}$).

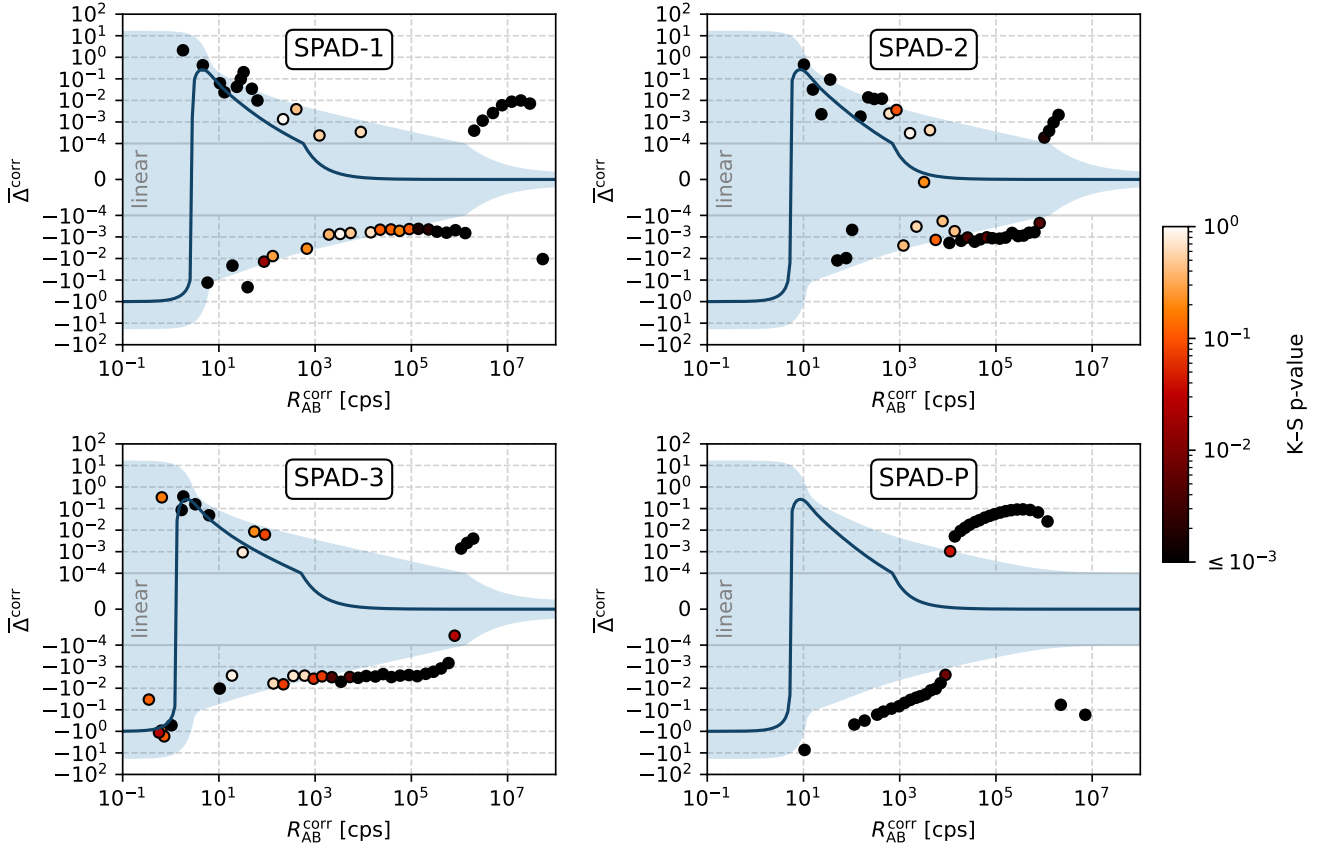


FIG. 11. Measured average nonlinearities after all detection rates are corrected for dead-time and dark-count effects (F2) based on the best-fit values given in Table III below. The points represent 30-sample averages; the solid lines are the theoretical mean values assuming the model (F1) holds; the blue area is a 95% confidence interval for the average values. Point color shows the Kolmogorov–Smirnov p-value, which tests whether the 30 constituent samples come from the expected distribution. Dark points are very unlikely to occur under the presumed model.

the average value and the distribution of the 30 samples for each point. The average nonlinearity is compared to a 95% confidence interval, and the Kolmogorov–Smirnov (KS) p-value of the distribution is denoted by the point color. The p-value is a probability that, assuming the model holds, we would obtain “worse” data than those measured, as parameterized by the KS statistic (see Statistical Methods below). Very low p-values show that statistical errors alone are unlikely to explain the data.

Many points show a disagreement with the theoretical model, with the difference standing out more in comparison to uncorrected data (Fig. 12), especially for $R_{\text{AB}}^{\text{det}} \gtrsim 10^6$ cps.

Accordingly, the basic model (F1) does not provide a satisfactory explanation of the measured data, so we should justify its use as opposed to other dead-time models, and quantify the effect of afterpulsing.

2. Dead time models

The effect of dead time in Geiger-mode SPADs is akin to Geiger–Müller (GM) counters [56–60, 67–71]. Two basic types of idealized models for dead time have been defined [57, 58, 68]. Namely, it is the paralyzable dead time τ_{P} model

$$f_{\text{P}}(R) = (R + R_0) \exp(-(R + R_0) \tau_{\text{P}}), \quad (\text{F3})$$

and the non-paralyzable dead time τ_{NP} model (F1). For the non-paralyzable case, each *registered* detection is followed by dead time, during which no further events are registered. In the paralyzable case, dead time follows every photon absorption, even those that occur within a previous dead time and are not otherwise recorded. This case covers the fact that secondary detections in GM tubes still require quenching, but are not recognized due to low voltage output.

In the case of GM counters, single-parameter dead-time models are just an approximation. Hybrid models were proposed by combining paralyzable and non-paralyzable dead times [61]. There are two variants; the NP-P model

$$f_{\text{NP-P}}(R) = \frac{(R + R_0) \exp(-(R + R_0) \tau_{\text{P}})}{1 + (R + R_0) \tau_{\text{NP}}}, \quad (\text{F4})$$

and the P-NP model [59, 72]

$$f_{\text{P-NP}}(R) = \frac{(R + R_0) \exp(-(R + R_0) \tau_{\text{P}})}{1 + (R + R_0) \tau_{\text{NP}} \exp(-(R + R_0) \tau_{\text{P}})}. \quad (\text{F5})$$

We have tested whether these theoretical models can be used empirically to fit the measured nonlinearity data. We found that all hybrid-model fits converge to either the paralyzable or non-paralyzable case. Fig. 12 shows both of these response models applied to the measured nonlinearity of all detectors. A complete list of the measured parameters and best-fit parameters is given in Table III.

As in the main text, we evaluated χ^2 to demonstrate that investigated models significantly deviate from the measured nonlinearity. In Table IV, we show the chi-squared per one degree of freedom, χ^2/ν , where ν is the number of data points minus the number of fitting parameters.

Both the χ^2 values and the plots in Fig. 12 show that the paralyzable and hybrid models do not offer a better explanation of the data; nor can they satisfactorily match the trend in the middle of the graphs of SPAD-1–3, where all nonlinearities seem to be systematically lower.

3. Afterpulsing

Actively quenched SPADs exhibit afterpulsing and twilight pulsing that affect the mean detection rate [36]. Both effects can be evaluated numerically [73], or – if we neglect the temporal distribution of afterpulses – an approximate rate formula can be used [36],

$$f_{\text{AP}}(R) = \left(\left[\frac{1}{(R + R_0)} - \alpha \right] e^{-\langle n_{\text{AP}} \rangle} + \tau_{\text{NP}} \right)^{-1}. \quad (\text{F6})$$

The new parameters are the mean number of afterpulses per detection $\langle n_{\text{AP}} \rangle$, and the twilight-pulse proportionality constant α that introduces rate dependence. As one would expect, when both of these parameters are zero, the formula (F6) is reduced to the basic non-paralyzable model (F1).

The key observation here is parameter degeneracy. In the formula (F6), the effect of afterpulsing can be substituted by adjusting the dead time and dark count variables in (F1). If we put the model parameters in square brackets, the equivalence can be expressed as

$$\begin{aligned} & f_{\text{AP}}(R) \left[R_0, \tau_{\text{NP}}, \langle n_{\text{AP}} \rangle, \alpha \right] \\ & \equiv f_{\text{NP}}(R/e^{-\langle n_{\text{AP}} \rangle}) \left[R_0/e^{-\langle n_{\text{AP}} \rangle}, \tau_{\text{NP}} - \alpha e^{-\langle n_{\text{AP}} \rangle} \right]. \end{aligned} \quad (\text{F7})$$

Let us now substitute both rate models into nonlinearity (1), assuming balanced splitting $R_{\text{A}}^{\text{det}} = R_{\text{B}}^{\text{det}}$ and the parameter equivalence (F7),

$$\Delta = \frac{2R_{\text{A}}^{\text{det}}}{R_{\text{AB}}^{\text{det}}} - 1 = \frac{2f[\frac{1}{2}f^{-1}(R_{\text{AB}}^{\text{det}})]}{R_{\text{AB}}^{\text{det}}} - 1. \quad (\text{F8})$$

One finds that $\Delta_{\text{AP}} \equiv \Delta_{\text{NP}}$, which follows from the equivalence (F7) and the scaling of R by a linear factor there. The principle is that both f_{AP}^{-1} and f_{NP}^{-1} yield incident rates that differ by the same linear factor, and their ratio does not change upon the multiplication by 1/2. A subsequent application of f therefore gives identical rates for both models. As a result, all fitted models are identical and yield the same χ^2 either with or without afterpulsing.

A further consideration would be a more complex afterpulsing model that considers the temporal distribution

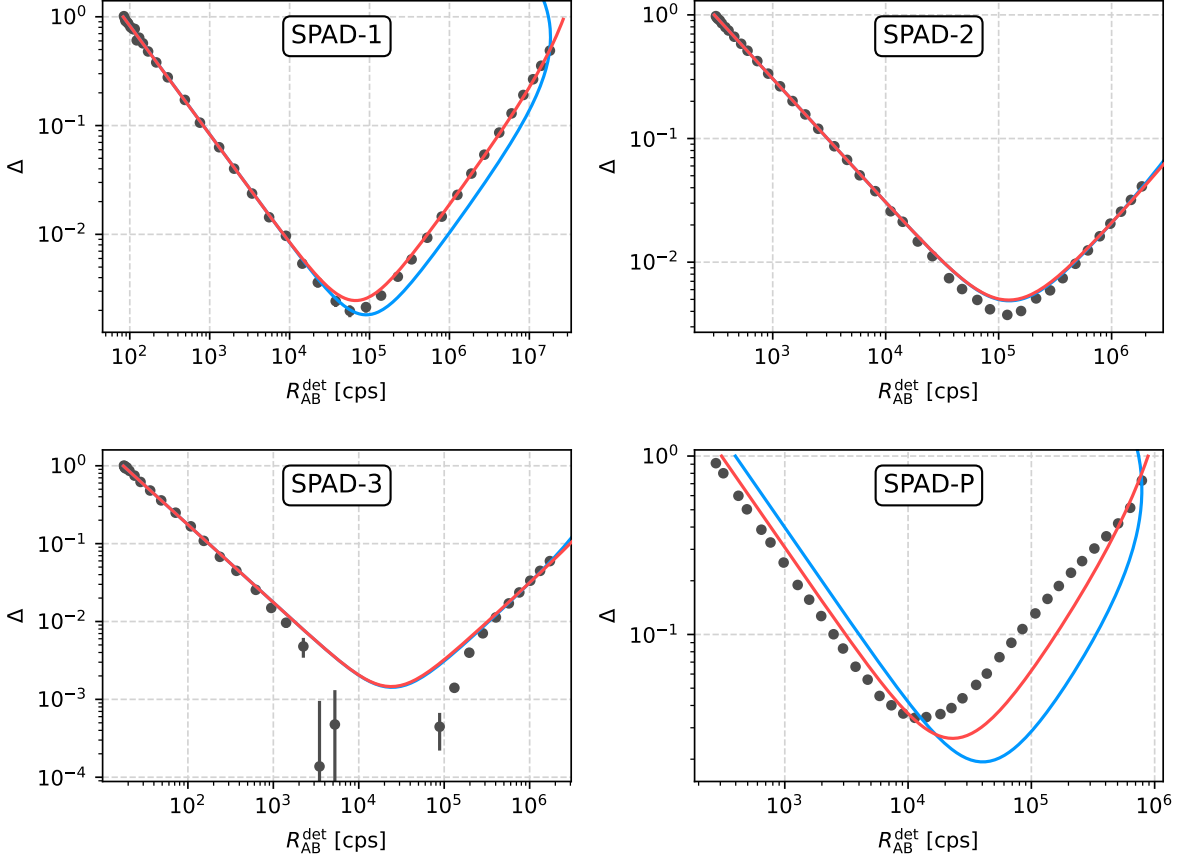


FIG. 12. Nonlinearity data fits using two models: the τ_{NP} model (red), and the τ_P model (blue). Note the right-side turning point of the paralyzable model (blue), which is a consequence of non-monotonous response to illumination.

	measured		τ_{NP} model		τ_P model		τ_{NP} - τ_P model	τ_P - τ_{NP} model
	R_0 [cps]	τ_R [ns]	R_0 [cps]	τ_{NP} [ns]	R_0 [cps]	τ_P [ns]		
SPAD-1	88(3)	29.5(5)	83(4)	36.7(1)	80(40)	20.0(1)	τ_{NP} model	τ_{NP} model
SPAD-2	314(5)	47.0(5)	304(2)	40.2(4)	304(1)	38.9(3)	τ_P model	τ_P model
SPAD-3	20(2)	56.6(6)	17.5(7)	61(1)	17.5(6)	58.2(9)	τ_P model	τ_P model
SPAD-P	264(1)	517(6)	300(200)	1130(20)	400(500)	467	τ_{NP} model	τ_{NP} model

TABLE III. Comparison of directly measured dark counts R_0 and recovery times τ_R , and dark counts and dead times τ_{NP} , τ_P , that were the best fits of individual response models. The last two columns show which scheme the hybrid models converge to.

	χ^2/ν	τ_{NP} model	τ_P model
SPAD-1	250	27000	
SPAD-2	12	8.4	
SPAD-3	40	31	
SPAD-P	9.8×10^4	1.1×10^6	

TABLE IV. Evaluated χ^2/ν values of the fitted theoretical response models for tested SPADs.

unsuitable for least-squares fitting. However, the difference between this full model Δ_{full} and the simple model (F6) can be evaluated for an example case. In Fig. 13, the difference is shown for SPAD-1 based on the afterpulsing data measured in Ref. [36]. Note that we have already established the equivalency of (F1) and (F6), so we can conclude that the full model introduces a very small correction to the basic model we used to fit the data.

of afterpulses [36]. This model is based on computationally demanding Monte-Carlo simulations and is therefore

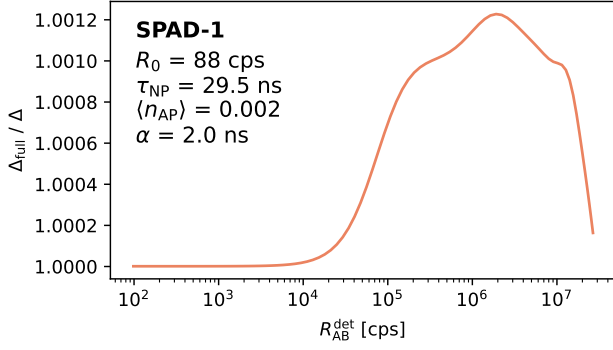


FIG. 13. The full afterpulsing model is compared to the simple model (F6), and thus to an equivalent basic model (F1) via (F7). The difference is shown for SPAD-1. It corresponds to a relative change of the fits depicted in Fig. 12 if a full afterpulsing correction was made.

4. Discussion of the models

An example case of an actively quenched SPAD, represented by SPAD-1, shows that an afterpulsing correction to our nonlinearity model would yield a relative difference of $\approx 0.1\%$ in Δ . A slightly simplified afterpulsing correction that can be used for data fitting yields no difference from the basic model. For this reason, we can conclude that afterpulses do not play a role in fitting the nonlinearity data of actively quenched SPADs.

The other detectors exhibit a much more complex behavior. Passively quenched SPADs exhibit paralyzable dead time, but also a rising efficiency curve after each detection [74], which makes the model too complex to be parameterized by a few measurable quantities.

SNSPDs show no afterpulsing, but, to our knowledge, their (non-)paralyzability has not been confirmed. Additionally, both SNSPDs and passively quenched SPADs exhibit changing efficiency after each detection, an effect that is both non-negligible and complex. In the case of SNSPDs, the single-photon and two-photon efficiencies also depend on the bias current. For these reasons, no standard rate model has been formulated that would be sufficiently accurate.

Upon exploration of certain empirical models combining non-paralyzable and paralyzable dead time, we found that none of them offer a significant advantage over the basic non-paralyzable model. SPAD-1–3 are non-paralyzable. SPAD-2 and SPAD-3 are better fitted with the paralyzable model, but the difference is very small, as can be seen from Fig. 12. SPAD-P is significantly better fitted by the non-paralyzable model. Consequently, we use a single model (F1) for all SPADs in the manuscript.

Appendix G: Statistical methods

This section elaborates on the statistical methods used to analyze and fit the SPAD data.

Due to the integration time $T = 20$ s, all the measured numbers of counts are $R^{\text{det}}T > 300$, which is sufficient for the normal approximation of the Poisson distribution. We therefore assume that all acquired count rates are normally distributed $\mathcal{N}(\theta, \sigma^2)$ with variance σ^2 (C5) as a function of a mean-value parameter θ ,

$$R^{\text{det}} \sim \mathcal{N}(\theta, (1 - \theta\tau_{\text{NP}})^2\theta/T). \quad (\text{G1})$$

We also assume that nonlinearity Δ , as a function of these rates, is also normally distributed, which requires the standard deviations to be small enough with respect to the mean values. The estimation of Δ is then carried out based on $N = 30$ samples. Due to the normality of the data, a least-squares fit of the model can be performed (Fig. 12).

However, when applying the correction (F2) on the data, the normality of Δ ceases to hold. This happens when the detection rate approaches the background rate, as then the corrected value fluctuates significantly compared to the mean value. For such low rates, dead time correction can be neglected and $R^{\text{corr}} \approx R^{\text{det}} - R_0$,

$$R^{\text{corr}} \sim \mathcal{N}(R, (R + R_0)/T) \quad \text{for } R \ll 1/\tau_{\text{NP}}, \quad (\text{G2})$$

where R denotes the incident rate. Due to Poissonian fluctuations of the dark counts, the corrected values can also end up negative. The probability density of

$$\Delta^{\text{corr}} = \frac{R_A^{\text{corr}} + R_B^{\text{corr}}}{R_{\text{AB}}^{\text{corr}}} - 1 \quad (\text{G3})$$

can be computed from (G2) by using the probability-density transformations

$$p_{(Z=X+Y)}(z) = \int_{-\infty}^{\infty} p_X(t)p_Y(z-t)dt, \quad (\text{G4})$$

$$p_{(Z=X/Y)}(z) = \int_{-\infty}^{\infty} p_X(zt)p_Y(t)|t|dt. \quad (\text{G5})$$

For $R \rightarrow 0$, the distribution of Δ^{corr} tends towards the Lorentz distribution with undefined variance, so that one cannot employ the central limit theorem to arrive at estimations of N -sample averages. As per (G4), the probability density of $\sum_{i=1}^N \Delta_i^{\text{corr}}$ is computed numerically by $(N-1)$ successive convolutions. This allows plotting the mean value and confidence intervals shown in Fig. 11, as well as evaluating the Kolmogorov–Smirnov statistic.

For $R \gg 0$, the distribution of Δ^{corr} can be regarded as normal, with its standard deviation obtained by locally linear propagation of (G1). However, as we are concerned with small values of Δ , we need to account for a bias in the mean value.

We note that all the measured rates in (G3) are independent, and the scheme is balanced, $\langle R_A^{\text{corr}} \rangle = \langle R_B^{\text{corr}} \rangle$,

and so

$$\langle \Delta^{\text{corr}} \rangle = 2 \langle R_A^{\text{corr}} \rangle \left\langle \frac{1}{R_{\text{AB}}^{\text{corr}}} \right\rangle - 1. \quad (\text{G6})$$

We employ the function (F2), where R_i^{det} is a normal-distributed variable described by (G1). The mean values θ_i for $i = A, \text{AB}$ are given by the function (F1), and the incident rate is R for $i = \text{AB}$ and $R/2$ for $i = A$. The main source of the bias is nonlinear dependence of the averaging terms on the random variables. We expand the averaging terms in a Taylor series,

$$f(R_i^{\text{det}}) \approx \sum_{n=0}^2 \left(\frac{\partial f}{\partial R_i^{\text{det}}} \right) (\theta_i) \frac{(R_i^{\text{det}} - \theta_i)^n}{n!}, \quad (\text{G7})$$

where it is sufficient to stop at the quadratic term. Averaging over $R_i^{\text{det}} \sim \mathcal{N}(\theta_i, \sigma_i^2)$ yields non-zero only for even $n = 2k$:

$$\left\langle \frac{(R_i^{\text{det}} - \theta_i)^{2k}}{(2k)!} \right\rangle = \frac{(\sigma_i^2/2)^k}{k!}. \quad (\text{G8})$$

We can also safely assume a short dead time and low background — $\tau \ll T$ and $\tau R_0 \ll 1$. This all results in

$$\langle \Delta^{\text{corr}} \rangle \approx \frac{R + R_0}{TR^2}, \quad (\text{G9})$$

which holds well for $R \gtrsim R_0$.

The above methods allow us to establish the probability distribution of $\overline{\Delta}^{\text{corr}} = \frac{1}{N} \sum_{i=1}^N \Delta_i^{\text{corr}}$ for the whole range of incident rates R . Then, one way of testing the validity of the data is the confidence interval of $\overline{\Delta}^{\text{corr}}$. A second test evaluates whether the samples Δ^{corr} conform to the expected distribution. However, due to non-normality, it would be difficult to evaluate measures based on multivariate probability density akin to χ^2 . Instead, we compare cumulative distributions.

The Kolmogorov–Smirnov statistic D_N is defined as the maximum difference between the empirical and theoretical cumulative distributions. For a certain $R_{\text{AB}}^{\text{det}}$, let the number of samples of Δ^{corr} lower than Δ be $n(\Delta)$. Then, the empirical cumulative distribution is $S_N(\Delta) = n(\Delta)/N$ with $S_N \in [0, 1]$. Let the theoretical cumulative distribution be $S(\Delta) = \text{Pr}[\Delta^{\text{corr}} < \Delta]$. We compare them by defining the statistic

$$D_N := \sup_{\Delta} |S_N(\Delta) - S(\Delta)|. \quad (\text{G10})$$

Then, for many samples, as $N \rightarrow \infty$, the quantity $(\sqrt{N}D_N)$ follows a known distribution assuming $S(\Delta)$ holds [75]. This quantity can therefore be evaluated for each set of N measurements, as depicted in Fig. 11. The p-value is then the probability $\text{Pr}[D_N > D_N^{\text{meas}}]$, which tests the null hypothesis that the data conform to the theoretical model.

-
- [1] V. Giovannetti, S. Lloyd, and L. Maccone, Advances in quantum metrology, *Nat. Photonics* **5**, 222 (2011).
- [2] K. R. Motes, J. P. Olson, E. J. Rabeaux, J. P. Dowling, S. J. Olson, and P. P. Rohde, Linear optical quantum metrology with single photons: Exploiting spontaneously generated entanglement to beat the shot-noise limit, *Phys. Rev. Lett.* **114**, 170802 (2015).
- [3] The LIGO Scientific Collaboration, Enhanced sensitivity of the LIGO gravitational wave detector by using squeezed states of light, *Nat. Photonics* **7**, 613 (2013).
- [4] S. Slussarenko, M. M. Weston, H. M. Chrzanowski, L. K. Shalm, V. B. Verma, S. W. Nam, and G. J. Pryde, Unconditional violation of the shot-noise limit in photonic quantum metrology, *Nat. Photonics* **11**, 700 (2017).
- [5] G. Brida, M. Genovese, and I. Ruo Berchera, Experimental realization of sub-shot-noise quantum imaging, *Nat. Photonics* **4**, 227 (2010).
- [6] M. A. Taylor, J. Janousek, V. Daria, J. Knittel, B. Hage, H.-A. Bachor, and W. P. Bowen, Biological measurement beyond the quantum limit, *Nat. Photonics* **7**, 229 (2013).
- [7] T. Ono, R. Okamoto, and S. Takeuchi, An entanglement-enhanced microscope, *Nat Commun* **4**, 1 (2013).
- [8] Y. Israel, R. Tenne, D. Oron, and Y. Silberberg, Quantum correlation enhanced super-resolution localization microscopy enabled by a fibre bundle camera, *Nat Commun* **8**, 1 (2017).
- [9] P.-A. Moreau, E. Toninelli, T. Gregory, and M. J. Padgett, Imaging with quantum states of light, *Nat. Rev. Phys.* **1**, 367 (2019).
- [10] D. A. Kalashnikov, A. V. Paterova, S. P. Kulik, and L. A. Krivitsky, Infrared spectroscopy with visible light, *Nat. Photonics* **10**, 98 (2016).
- [11] R. Whittaker, C. Erven, A. Neville, M. Berry, J. L. O’Brien, H. Cable, and J. C. F. Matthews, Absorption spectroscopy at the ultimate quantum limit from single-photon states, *New J. Phys.* **19**, 023013 (2017).
- [12] E. Jakeman and J. Rarity, The use of pair production processes to reduce quantum noise in transmission measurements, *Opt. Commun.* **59**, 219 (1986).
- [13] J. Sabines-Chesterking, R. Whittaker, S. K. Joshi, P. M. Birchall, P. A. Moreau, A. McMillan, H. V. Cable, J. L. O’Brien, J. G. Rarity, and J. C. F. Matthews, Sub-shot-noise transmission measurement enabled by active feed-forward of heralded single photons, *Phys. Rev. Applied* **8**, 014016 (2017).
- [14] E. Losero, I. Ruo-Berchera, A. Meda, A. Avella, and M. Genovese, Unbiased estimation of an optical loss at the ultimate quantum limit with twin-beams - Scientific Reports, *Sci. Rep.* **8**, 1 (2018).
- [15] J. Sabines-Chesterking, A. R. McMillan, P. A. Moreau, S. K. Joshi, S. Knauer, E. Johnston, J. G. Rarity, and J. C. F. Matthews, Twin-beam sub-shot-noise raster-scanning microscope, *Opt. Express* **27**, 30810 (2019).
- [16] U. Sinha, C. Couteau, T. Jennewein, R. Laflamme, and G. Weihs, Ruling out multi-order interference in quantum mechanics, *Science* **329**, 418 (2010).

- [17] I. Söllner, B. Gschösser, P. Mai, B. Pressl, Z. Vörös, and G. Weihs, Testing Born's Rule in Quantum Mechanics for Three Mutually Exclusive Events, *Found. Phys.* **42**, 742 (2012).
- [18] O. S. Magaña-Loaiza, I. De Leon, M. Mirhosseini, R. Fickler, A. Safari, U. Mick, B. McIntyre, P. Banzer, B. Rodenburg, G. Leuchs, and R. W. Boyd, Exotic looped trajectories of photons in three-slit interference - *Nature Communications*, *Nat Commun* **7**, 1 (2016).
- [19] T. Kauten, R. Keil, T. Kaufmann, B. Pressl, Č. Brukner, and G. Weihs, Obtaining tight bounds on higher-order interferences with a 5-path interferometer, *New J. Phys.* **19**, 033017 (2017).
- [20] J. P. Cotter, C. Brand, C. Knobloch, Y. Lilach, O. Cheshnovsky, and M. Arndt, In search of multipath interference using large molecules, *Sci. Adv.* **3**, e1602478 (2017).
- [21] G. Rengaraj, U. Prathwiraj, S. N. Sahoo, R. Somashekhar, and U. Sinha, Measuring the deviation from the superposition principle in interference experiments, *New J. Phys.* **20**, 063049 (2018).
- [22] C. M. Natarajan, M. G. Tanner, and R. H. Hadfield, Superconducting nanowire single-photon detectors: physics and applications, *Supercond. Sci. Technol.* **25**, 063001 (2012).
- [23] A. Migdall, S. V. Polyakov, J. Fan, and J. C. Bienfang, *Single-Photon Generation and Detection* (Academic Press, 2013).
- [24] C. J. Chunnillall, I. P. Degiovanni, S. Kück, I. Müller, and A. G. Sinclair, Metrology of single-photon sources and detectors: a review, *Opt. Eng.* **53**, 081910 (2014).
- [25] R. H. Hadfield and G. Johansson, eds., *Superconducting Devices in Quantum Optics* (Springer International Publishing, 2016).
- [26] I. Esmail Zadeh, J. Chang, J. W. N. Los, S. Gyger, A. W. Elshaari, S. Steinhauer, S. N. Dorenbos, and V. Zwiller, Superconducting nanowire single-photon detectors: A perspective on evolution, state-of-the-art, future developments, and applications, *Appl. Phys. Lett.* **118**, 190502 (2021).
- [27] A. R. Schaefer, E. F. Zalewski, and J. Geist, Silicon detector nonlinearity and related effects, *Appl. Opt.* **22**, 1232 (1983).
- [28] M. Tanabe, K. Amemiya, T. Numata, and D. Fukuda, Spectral supralinearity prediction of silicon photodiodes in the near-infrared range, *Appl. Opt.* **54**, 10705 (2015).
- [29] M. Tanabe, K. Amemiya, T. Numata, and D. Fukuda, Spectral supralinearity of silicon photodiodes in visible light due to surface recombination, *Appl. Opt.* **55**, 3084 (2016).
- [30] A. J. Kerman, D. Rosenberg, R. J. Molnar, and E. A. Dauler, Readout of superconducting nanowire single-photon detectors at high count rates, *J. Appl. Phys.* **113**, 144511 (2013).
- [31] F. Marsili, M. J. Stevens, A. Kozorezov, V. B. Verma, C. Lambert, J. A. Stern, R. D. Horansky, S. Dyer, S. Duff, D. P. Pappas, A. E. Lita, M. D. Shaw, R. P. Mirin, and S. W. Nam, Hotspot relaxation dynamics in a current-carrying superconductor, *Phys. Rev. B* **93**, 094518 (2016).
- [32] M. Stipčević, D. Wang, and R. Ursin, Characterization of a commercially available large area, high detection efficiency single-photon avalanche diode, *J. Light. Technol.* **31**, 3591 (2013).
- [33] V. Kornilov, Effects of dead time and afterpulses in photon detector on measured statistics of stochastic radiation, *J. Opt. Soc. Am. A* **31**, 7 (2014).
- [34] F. Wang, W. Chen, Y. Li, D. He, C. Wang, Y. Han, S. Wang, Z. Yin, and Z. Han, Non-markovian property of afterpulsing effect in single-photon avalanche detector, *J. Light. Technol.* **34**, 3610 (2016).
- [35] M. A. Wayne, J. C. Bienfang, and S. V. Polyakov, Simple autocorrelation method for thoroughly characterizing single-photon detectors, *Opt. Express* **25**, 20352 (2017).
- [36] I. Straka, J. Grygar, J. Hloušek, and M. Ježek, Counting statistics of actively quenched SPADs under continuous illumination, *J. Light. Technol.* **38**, 4765 (2020).
- [37] M. Keshavarz Akhlaghi and A. H. Majedi, Semiempirical modeling of dark count rate and quantum efficiency of superconducting nanowire single-photon detectors, *IEEE Transactions on Applied Superconductivity* **19**, 361 (2009).
- [38] M. K. Akhlaghi, A. H. Majedi, and J. S. Lundeen, Nonlinearity in single photon detection: modeling and quantum tomography, *Opt. Express* **19**, 21305 (2011).
- [39] A. Luis and L. L. Sánchez-Soto, Complete characterization of arbitrary quantum measurement processes, *Phys. Rev. Lett.* **83**, 3573 (1999).
- [40] J. Fiurášek, Maximum-likelihood estimation of quantum measurement, *Phys. Rev. A* **64**, 024102 (2001).
- [41] J. S. Lundeen, A. Feito, H. Coldenstrodt-Ronge, K. L. Pregnell, Ch. Silberhorn, T. C. Ralph, J. Eisert, M. B. Plenio, and I. A. Walmsley, Tomography of quantum detectors, *Nat. Phys.* **5**, 27 (2009).
- [42] G. Brida, L. Ciavarella, I. P. Degiovanni, M. Genovese, L. Lolli, M. G. Mingolla, F. Piacentini, M. Rajteri, E. Taralli, and M. G. A. Paris, Quantum characterization of superconducting photon counters, *New J. Phys.* **14**, 085001 (2012).
- [43] C. M. Natarajan, L. Zhang, H. Coldenstrodt-Ronge, G. Donati, S. N. Dorenbos, V. Zwiller, I. A. Walmsley, and R. H. Hadfield, Quantum detector tomography of a time-multiplexed superconducting nanowire single-photon detector at telecom wavelengths, *Opt. Express* **21**, 893 (2013).
- [44] M. Cooper, M. Karpiński, and B. J. Smith, Local mapping of detector response for reliable quantum state estimation, *Nat Commun* **5**, 4332 (2014).
- [45] S. Grandi, A. Zavatta, M. Bellini, and M. G. A. Paris, Experimental quantum tomography of a homodyne detector, *New J. Phys.* **19**, 053015 (2017).
- [46] S. Izumi, J. S. Neergaard-Nielsen, and U. L. Andersen, Tomography of a feedback measurement with photon detection, *Phys. Rev. Lett.* **124**, 070502 (2020).
- [47] S. Ferrari, V. Kovalyuk, A. Vetter, C. Lee, C. Rockstuhl, A. Semenov, G. Gol'tsman, and W. Pernice, Analysis of the detection response of waveguide-integrated superconducting nanowire single-photon detectors at high count rate, *Appl. Phys. Lett.* **115**, 101104 (2019).
- [48] C. L. Sanders, Accurate Measurements of and Corrections for Nonlinearities in Radiometers, *J. Res. Nat. Bur. Stand. Sec. A: Phys. Ch.* **76A**, 437 (1972).
- [49] J. S. Preston and L. H. McDermott, The illumination-response characteristics of vacuum photoelectric cells of the elster-geitel type, *Proc. Phys. Soc.* **46**, 256 (1934).
- [50] L. Coslivi and F. Righini, Fast determination of the nonlinearity of photodetectors, *Appl. Opt.* **19**, 3200 (1980).
- [51] R. D. Saunders and J. B. Shumaker, Automated radiometric linearity tester, *Appl. Opt.* **23**, 3504 (1984).

- [52] A. Haapalinna, T. Kübarsepp, P. Kärhä, and E. Ikonen, Measurement of the absolute linearity of photodetectors with a diode laser, *Meas. Sci. Technol.* **10**, 1075 (1999).
- [53] D.-J. Shin, S. Park, K.-L. Jeong, S.-N. Park, and D.-H. Lee, High-accuracy measurement of linearity of optical detectors based on flux addition of LEDs in an integrating sphere, *Metrologia* **51**, 25 (2013).
- [54] T. Kauten, B. Pressl, T. Kaufmann, and G. Weihs, Measurement and modeling of the nonlinearity of photo-voltaic and Geiger-mode photodiodes, *Rev. Sci. Instrum.* **85**, 063102 (2014).
- [55] M. Ware, A. Migdall, J. C. Bienfang, and S. V. Polyakov, Calibrating photon-counting detectors to high accuracy: background and deadtime issues, *J. Mod. Opt.* **54**, 361 (2007).
- [56] W. Feller, *On probability problems in the theory of counters* (Courant anniversary volume, New York, 1948) pp. 105–115.
- [57] R. D. Evans, *The atomic nucleus, Applications of Poisson statistics to some instruments used in nuclear physics* (McGraw-Hill, New York, 1955) Chap. 28, p. 785.
- [58] G. F. Knoll, *Radiation detection and measurement* (John Wiley & Sons, New York, 1989) p. 120.
- [59] J. W. Müller, Generalized dead times, *Nucl. Instrum. Methods. Phys. Res. B* **301**, 543 (1991).
- [60] R. P. Gardner and L. Liu, On extending the accurate and useful counting rate range of GM counter detector systems, *Appl. Radiat. Isot.* **48**, 1605 (1997).
- [61] S. H. Lee and R. P. Gardner, A new G-M counter dead time model, *Appl. Radiat. Isot.* **53**, 731 (2000).
- [62] M. A. Karami, L. Carrara, C. Niclass, M. Fishburn, and E. Charbon, RTS noise characterization in single-photon avalanche diodes, *IEEE Electron Device Letters* **31**, 692 (2010).
- [63] J. Hloušek, I. Straka, and M. Ježek, <https://github.com/PepaHloušek/Nonlinearity> (2021), Experimental observation of anomalous supralinear response of single-photon detectors – GitHub repository.
- [64] QOLO-made 30 ms optical shutter using RC servo (2012), <http://quantum.opticsolomouc.org/archives/1177>.
- [65] Countex – QOLO-made counter and coincidence unit (2020), <http://quantum.opticsolomouc.org/archives/2412>.
- [66] D. Allan, Statistics of atomic frequency standards, *Proceedings of the IEEE* **54**, 221 (1966).
- [67] J. W. Müller, Dead-time problems, *Nucl. Instrum. Methods. Phys. Res. B* **112**, 47 (1973).
- [68] C. Levert and W. Scheen, Probability fluctuations of discharges in a geiger-müller counter produced by cosmic radiation, *Physica* **10**, 225 (1943).
- [69] G. E. Albert and L. Nelson, Contributions to the statistical theory of counter data, *The Annals of Mathematical Statistics* **24**, 9 (1953).
- [70] L. Takacs, On a probability problem in the theory of counters, *The Annals of Mathematical Statistics* **29**, 1257 (1958).
- [71] J. W. Muller, A simple derivation of the takacs formula, in *Rapport BIPM-88/3* (1988).
- [72] J. Lee, I. Kim, and H. Choi, On the dead time problem of a GM counter, *Appl. Radiat. Isot.* **67**, 1094 (2009).
- [73] I. Straka, J. Grygar, J. Hloušek, and M. Ježek, SPAD counting model (2020), <https://doi.org/10.24433/CO.8487128.v1>.
- [74] S. Cova, M. Ghioni, A. Lacaita, C. Samori, and F. Zappa, Avalanche photodiodes and quenching circuits for single-photon detection, *Appl. Opt.* **35**, 1956 (1996).
- [75] W. Feller, On the Kolmogorov–Smirnov Limit Theorems for Empirical Distributions, *Annals of Mathematical Statistics* **19**, 117 (1948).